



Microwave Plasma Jet in Water: Characterization and Feasibility to Wastewater Treatment

Ahmad Hamdan^{1,2} · Jing-Lin Liu^{1,3} · Min Suk Cha¹

Received: 10 May 2018 / Accepted: 2 July 2018 / Published online: 6 July 2018
© Springer Science+Business Media, LLC, part of Springer Nature 2018

Abstract

Plasma–liquid interactions have gained escalated interests over the last decade due to their potentials in many applications. The simultaneous generation of physicochemical phenomena of interest promotes itself to the top of the promising technologies for liquid processing. Here, we study the physics of a microwave plasma jet (MWPJ) submerged into water and its feasibility to wastewater treatment. We investigate the plasma and bubble dynamics using high-speed imaging. The effects of the argon flow rate, additive gas, and microwave power on the dynamics are examined highlighting the retreating behaviors of plasma channels due to the losses of electrons and power caused by nearby water surface. The addition of N₂ (<5%) to Ar flow results in an oscillatory motion of the foremost edge of the plasma channel. We characterize the submerged MWPJ using a time- and space-averaged optical emission spectroscopy. We found the dominant OH (A–X) molecular band and atomic Ar lines with pure Ar flow indicating the effective dissociation of water. Meanwhile, the addition of N₂ leads to an intense emission of NH (A–X) molecular band. Finally, we assess the submerged MWPJ as a viable method for water purification based on the degradation of methylene blue (popular model compound). We find a significant improvement in the efficiency by adding 1–3% of N₂ to the Ar, which should be attributed to a combined effects of NH radicals, having high redox potential, and the backward reactions of H₂O₂ to form OH radicals with NO and NO₂.

Keywords Microwave plasma · Plasma in water · Water treatment · High-speed imaging · Optical emission spectroscopy

✉ Ahmad Hamdan
ahmad.hamdan@umontreal.ca

Min Suk Cha
min.cha@kaust.edu.sa

¹ Clean Combustion Research Center (CCRC)/Physical Science and Engineering Division (PSE), King Abdullah University of Science and Technology (KAUST), Thuwal 23955, Saudi Arabia

² Groupe de physique des plasmas, Département de Physique, Université de Montréal, C.P. 6128, Succ. Centre-ville, Montréal, QC H3C 3J7, Canada

³ Dalian University of Technology, Dalian, China

Introduction

To date, numerous plasma sources have been developed and studied for liquid processing [1–3]. They can be classified into two categories: thermal and non-thermal plasma sources. Non-thermal plasmas, including pulsed-nanosecond discharge [4–6], dielectric barrier discharge [7, 8], and plasma jet [9], have been extensively investigated for liquid processing. Such plasmas have shown great potential for controlling the electron induced chemistry [2], because electron energy is selectively augmented while the gas temperature (i.e., the energy of heavy species) is somewhat unchanged. On the other hand, thermal plasmas such as plasma torches [10] and arc jets [11, 12] are known to utilize high temperature chemistry as well as plasma generated reactive species (electrons, ions, radicals, photons, etc.).

Gas temperature of non-thermal plasmas remains close to room temperature, even as the electron energy is relatively high (several eVs), which gives them an excellent ability to process temperature-sensitive materials such as polymers, biological liquids, and living cells [13–15]. However, despite their unique physical and chemical properties, non-thermal plasmas present some limitations in terms of yields (of process reactions) and/or plasma-device lifetime. When we take the example of in-liquid plasmas generated by nanosecond discharges, these discharges are generated with or without gaseous bubbles, and usually run in spark mode [16–18] (i.e., the plasma channel connects two electrodes) or in streamer mode [4–6] (i.e., the plasma channel is connected to one electrode). In the case of a spark mode, the plasma-electrode interaction is relatively strong, which leads to erosion issue [19–21] and reduces a lifetime of electrodes. In addition, a contamination of plasma treated liquid due to materials from electrode erosion may cause problems, particularly when the size of the particles is very small, and classical purification methods fail to remove them.

Another limitation is related to a process efficiency, which applies to both spark and streamer modes. Admitting the process efficiency is somewhat related with a plasma volume, when chemical and physical aspects of plasma are similar, relatively small in-liquid non-thermal plasmas' volumes [4, 6, 16] pull down process efficiencies and prevent the non-thermal in-liquid processes from being practically scaled up. Several methods to increase the plasma volume have been previously investigated. One of them is the discharge in biphasic media, either from a gas–liquid or liquid–liquid mixture. An example of this method is the injection of gaseous bubbles into a liquid to facilitate the breakdown and increase the plasma volume [18, 22, 23]. The results obtained with this method are quite remarkable in terms of selectivity [18, 24–26], which increases the efficiency in removing specific pollutants; however, the plasma volume still remains too small to significantly increase the global efficiency of the processes. In addition, when a size of gaseous bubble is comparable to the inter-electrodes distance, the electrode erosion is also significant [17, 18].

Contrary to non-thermal plasmas, thermal plasmas, such as torches and arc jets, provide a good efficiency by combining the chemical reactions induced by plasma species (electrons and ions) with those induced thermally. Our group has recently developed a submerged arc plasma jet to remove organic contaminant (phenol) from water [12], highlighting independent generation of plasma regardless of liquid properties and efficient removal of phenol due to increased plasma volume and its interaction with water. However, the erosion of the electrode could not be avoided, which caused a limited lifetime of the device to several hours as well as secondary contamination.

Although the family of microwave plasmas is classified sometimes as non-thermal plasma or as thermal plasma, depending on the microwave power, the physics of such

high-frequency plasma is well known. Recently, microwave discharges in dielectric liquids have been reviewed by Lebedev et al. [2]. Note that the principle of submerging the microwave plasma in water was proposed in 2012 during the *VIII International Workshop on Microwave discharges: Fundamentals and Applications* by Barkhudarov et al. [27]. Moreover, electrodeless microwave plasma jet (MWPJ), using a surfatron device, in contact with water was proposed by García et al. [28], and it has been tested for methylene blue degradation. Here, we present a submerged MWPJ in water. This setup has the advantages of (1) controlling plasma parameters independently irrespective of liquid properties, (2) free from electrode erosion, and (3) providing an efficient water treatment due to increased surface interaction between plasma and treated water as demonstrated in the previous study [12]. Because it is submerged in water, the plasma species can be transported to the entire volume of water due to turbulent mixing. Therefore, in addition to the direct interactions between water and short-lived species (electrons, ions, and photons), other long-lived species (radical, and metastable atoms and molecules) are allowed to interact with water. Such submerged electrodeless MWPJ is thus a promising setup for water treatment. In the present study, we investigate the physical characteristics of the submerged MWPJ highlighting the dynamic behaviors of both bubbles and plasma channels. In addition, in order to examine its feasibility to be applied in water treatment, methylene blue is selected as a simulated organic contaminant, which has many previous literatures to compare, and a degradation of methylene blue is presented. To detail the plasma, optical emission spectroscopy identifies plasma generated species and rotational temperatures of plasma particles.

Experimental Setup

A schematic of the experimental setup is shown in Fig. 1. It consists of a surfatron device and a microwave generator, a quartz tube to form a plasma with supplied gas, a water container, and diagnostic systems. The quartz tube is connected to the water container, a square-cylinder made by quartz, having 200 mL of distilled water in a 300-mL maximum volume (the volume of water is maintained for all tested conditions). The outer- and inner-diameter of the quartz tube are 6 and 4 mm, respectively, and the distance from the bottom of the water container to the quartz tube (plasma inlet) is 5 cm (Fig. 1b), thus the location

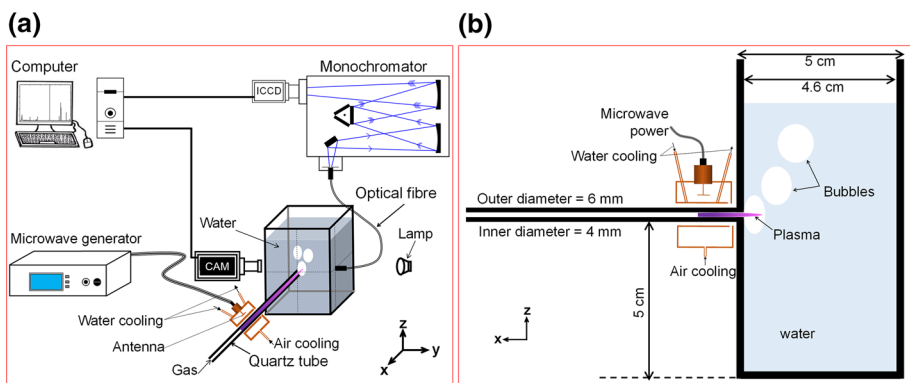


Fig. 1 Schematic of the experimental setup used to create submerged MWPJ: **a** 3D view and **b** 2D view

of the plasma inlet is ~ 5 cm below the surface of water. The surfatron (SURFATRON60, SAIREM) is positioned as close as possible to the water container, such that the injection length of a plasma jet to the water can be maximized.

A solid-state microwave generator (GMS200W, SAIREM) transmits the microwave at 2.45 GHz via a coaxial cable to the surfatron. A feeding gas (argon, with (or without) nitrogen or oxygen as an additive gas), with a purity of 99.999%, is supplied through the quartz tube using a mass flow controller. To generate the plasma, argon is used as the feeding gas with a flow rate of 1 L/min at a standard temperature and pressure condition (20 °C and 1 atm.) and at initial microwave power (μ WP) of 50 W. As seeding electrons are not enough to absorb the μ WP and ignite the plasma, we use a high frequency (~ 500 kHz) generator (BD-10ASV, ETP) to generate sparks close to the quartz tube providing thus extra electrons that can absorb the microwave power and sustain the plasma inside the quartz tube. Then, an operating conditions, such as a gas composition, gas flow rate, and μ WP are adjusted after the plasma ignition. Note that to maintain the plasma in a stable manner, the surfatron is cooled by chilled water supplied at 16 °C, and a forced dry air flow between the surfatron and the quartz tube to cool the latter.

To analyze bubble dynamics occurring with MWPJ injected into water, a high-speed imaging is adopted. A high-speed camera (Image Pro HS, LaVision) is placed in the x - z plane shown in Fig. 1, and a light-emitting diode (LED) lamp (SST-90, Luminus) is located on the other side of the camera to illuminate the area of interest. The exposure time and a framing rate are 0.47 ms and 2 kHz, respectively. An optical emission spectroscopy is also adopted to further investigate detailed characteristics of MWPJ in water, such as plasma species and temperature. A spectrometer (SP2750, Princeton Instruments) equipped with a grating (900 grooves/mm, blazed at visible), an optical fiber (LG-455-020-3, Princeton Instruments), and an ICCD camera (PI-MAX3, Princeton Instrument) is used. The width of the spectrometer's entrance slit is set at 100 μ m, and a resulted spectral resolution of the system is 0.036 nm.

In addition, to evaluate the applicability of the MWPJ for wastewater treatment, the removal of methylene blue (MB) in distilled water is investigated. The tested initial concentration of MB in distilled water is 50 mg/L, and the treated amount of MB contained water is also 200 mL. To estimate a removal efficiency of MB, an UV-Vis spectrophotometer (Genesys 10S, Thermo Scientific) is employed measuring the absorbance of light in a wavelength range from 350 to 1100 nm. As a result, a decolorization efficiency is determined based on the absorbance intensity at 663 nm, which represents MB. Note that, due to a measuring resolution of the spectrophotometer, the liquid samples are diluted 10 times with distilled water. The solution acidity (pH) and electrical conductivity are also measured by a pH-sensor (Inlab Expert Go-ISM, Mettler Toledo) and a conductivity-meter (Inlab 731-ISM, Mettler Toledo), respectively.

Results and Discussion

Physical Characterization of the Submerged MWPJ

High-speed imaging is used to investigate the simultaneous time evolution of a plasma channel and a bubble evaluating the effects of the gas flow rate and the μ WP. Figure 2 illustrates the instantaneous images of the plasma and the bubble at selected elapsed times. Initial time ($t=0$) indicates the moment right after a detachment of a previous bubble from the

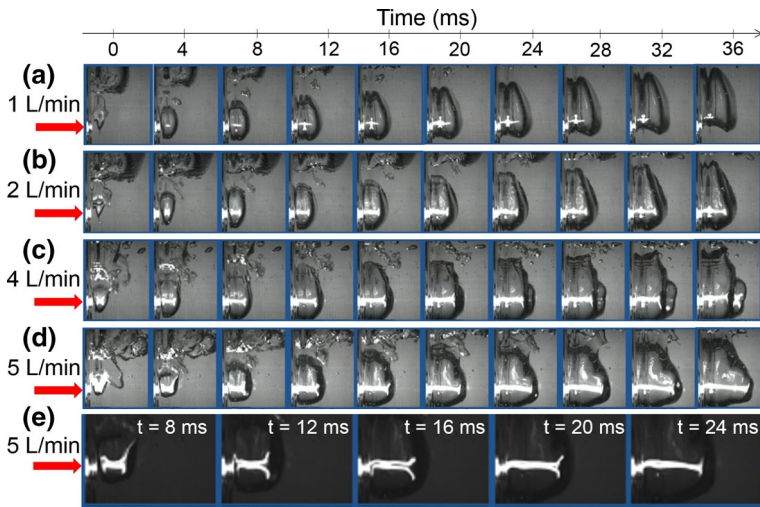


Fig. 2 Plasma–bubble dynamics for various Ar flow rates at $\mu\text{WP}=200\text{ W}$ and water volume = 200 mL: **a** the argon flow rate of 1, **b** 2, **c** 4, and **d** 5 L/min; **e** is with the same condition as (**d**) but retaken with a higher spatial resolution. The red arrow indicates the plasma inlet and flow direction

inlet of the plasma during a periodic cycle. Each row of the figure represents each tested flow rate of Ar as 1, 2, 4, and 5 L/min, respectively, while the μWP is fixed at 200 W (videos are available on demand). It should be noted that the plasma cannot propagate into a bubble with the Ar flow rate smaller than 0.5 L/min. As a consequence of the increased Ar flow rate, the bubble size increases, therefore, we observe the increased plasma length. In addition to the increased plasma length, an increase in the vertical thickness of the plasma is also observed. Particularly, for higher Ar flow rates (4 and 5 L/min), the plasma channel becomes filamentary at the foremost edge exhibiting the filaments propagate along the gas–water interface perpendicularly to the main horizontal plasma channels (Fig. 2e).

To characterize the dynamics of the plasma and the bubbles, the horizontal lengths of the discharge channel and the bubble are analyzed from the high-speed images, and the results are presented in Fig. 3. A monotonic increase in the bubble length is observed. The rate of increase slows down along the elapsed time because the rate of increase in bubble's volume, which is related to its cubic length, should be constant with the constant flow rate of Ar. When the bubble length reaches a critical length, the bubble detaches from the side wall and a new successive bubble starts forming repeating the cycle.

The plasma length first increases similarly to the bubble length, then, it decreases rapidly. For all tested flow rates, we observe increasing trend of the plasma length as the bubble length increases for a while, but at some instant, the foremost edge of the discharge channel starts to retreat, leading eventually to the total extinction of the plasma in the bubble. This behavior indicates complicated plasma dynamics inside the bubble coupled with water, although the MWPI into ambient air exhibits a steady plasma channel. We also find that, for the lowest flow rate tested (1 L/min), the plasma length is significantly shorter than the bubble length, indicating that the plasma channel cannot reach a bubble–liquid interface. For higher flow rates, the plasma length is comparable to that of the bubble for the initial phase of plasma development. However, a detailed explanation for all these observations cannot be made at this point. Note that the duration of the plasma emission seems to

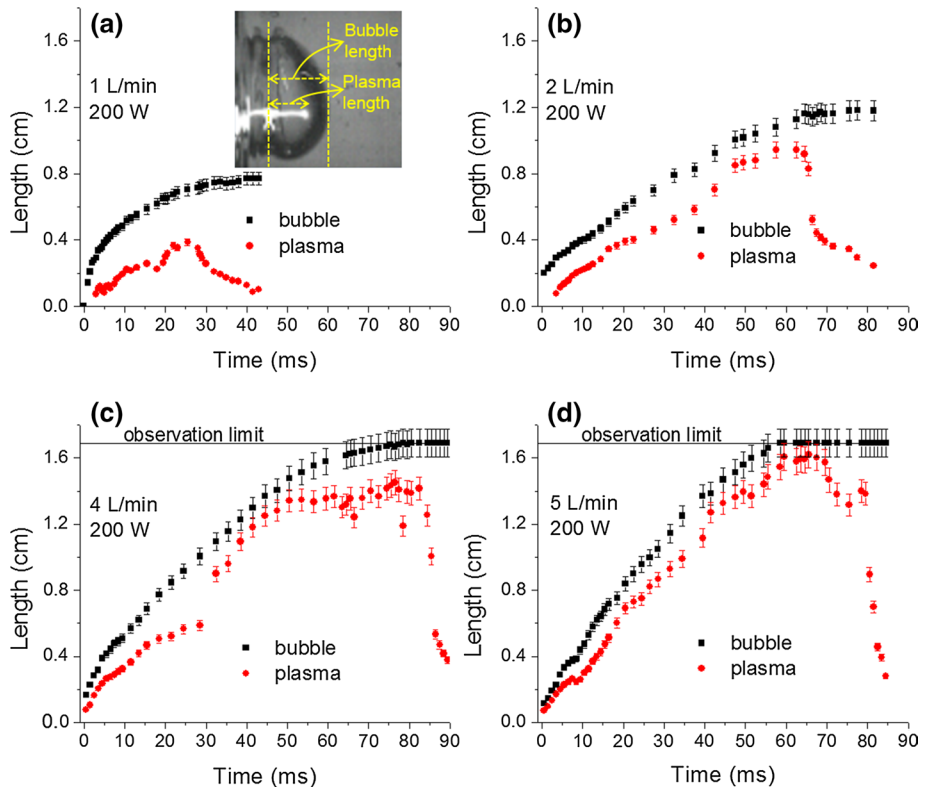


Fig. 3 Time evolution of the plasma length and bubble length for various Ar flow rates at $\mu\text{WP}=200$ W and water volume=200 mL: **a** with the argon flow rate of 1, **b** 2, **c** 4, and **d** 5 L/min. These results are obtained from processing the high-speed images. The inset of **(a)** shows the definition of the lengths; the plasma exit (left reference line) is determined based on the plane symmetry due to the reflection from the left side wall

increase with the flow rate, showing a saturated behavior over 4 L/min: ~ 45 and ~ 80 ms for 1 and 2 L/min, respectively, and saturated at ~ 90 ms for 4 and 5 L/min.

To understand the effect of μWP on the dynamics of plasma and bubbles, we vary the μWP from 200 down to 25 W at a fixed Ar flow rate at 2 L/min (Fig. 4).

In terms of the bubble length, we observe that μWP does not affect the final length of the bubble significantly for $\mu\text{WP} \geq 50$ W, say it is approximately 1.2 cm. However, for the lowest μWP , the bubble length is significantly reduced to ~ 0.84 cm at 25 W. Because the Ar flow rate is fixed at 2 L/min, the bubble length should be increased being proportional to μWP ; increased μWP implies increased volume of gas due to both temperature increase and evaporation of water into the bubble. Thus, the present result with the saturated bubble length indicates a non-spherical (anisotropic) evolution of the bubble caused by competition between horizontal jet momentum and vertical buoyant force.

The behaviors of the plasma length in the propagating regime of the plasma channel for $\mu\text{WP} \geq 50$ W are similar to each other (Figs. 3b, 4a–c), exhibiting a quasilinear increase until the plasma channel reaches its maximum length. For instance, the maximum lengths of the plasma channels are approximately 0.94, 0.89, 0.86, and 0.8 cm at $\mu\text{WP}=200, 150,$

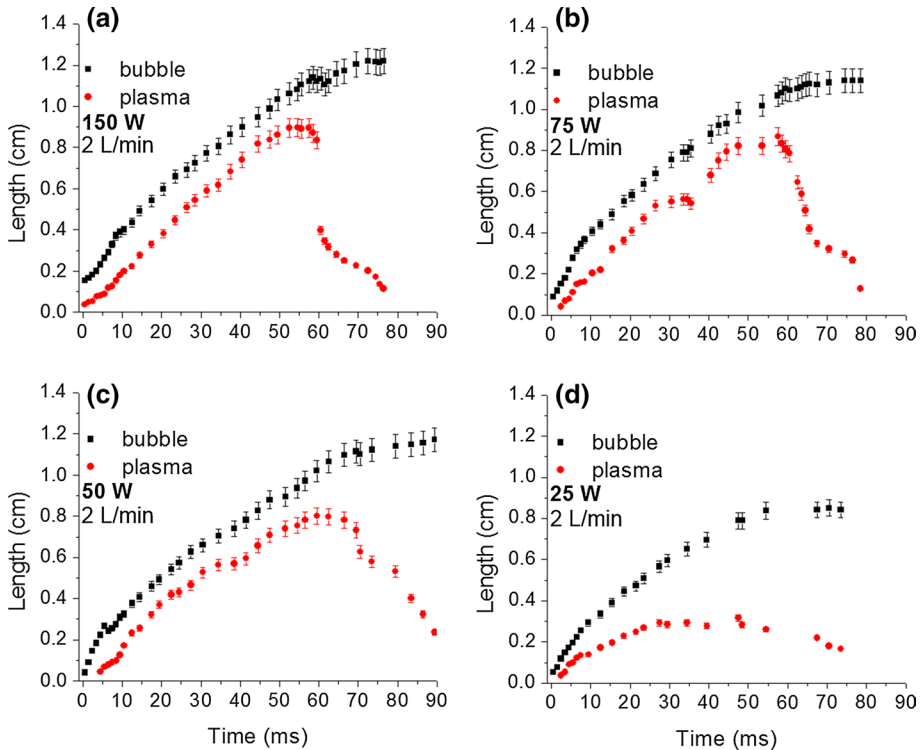


Fig. 4 Time evolution of the plasma length and bubble length for various μ WPs at the Ar flow rate is 2 L/min and water volume is 200 mL: **a** μ WP=150 W, **b** 75 W, **c** 50 W, and **d** 25 W

75, and 50 W, respectively, and each characteristic time to reach the maximum is around 62, 55, 55, and 60 ms. The gap distance between the edge of the plasma and the bubble–water interface keeps consistently at around 1 mm throughout the propagation irrespective of μ WP. However, at μ WP=25 W, the maximum plasma length is very short (~0.3 cm) demonstrating relatively large separation of the plasma edge from the bubble–water interface (by ~6 mm), although a quasilinear increase is also found in the propagating regime. However, the variation of the plasma length in the retreating regime is gradually changed as μ WP decreases: from a rapidly shrinking feature for a high μ WP to a slowly retreating plasma edge at a low μ WP. Note that the time durations of active plasma channels fall similarly in a range of 80–90 ms, regardless of μ WP.

A typical plasma length of the MWJP into ambient air is ~5 cm at the Ar flow rate of 2 L/min and μ WP=200 W, thus a continuous elongation of the plasma channel, up to the maximum bubble length was naturally expected. However, because the gas is injected horizontally, an anisotropic expansion and upward movement of a bubble, even before detachment, should cause a retreating edge of the plasma channel. An horizontal bubble expansion should be mostly due to the jet momentum, thus the bubble length should exhibit a saturated behavior where a horizontal jet momentum is zero at the bubble–liquid interface, for a given gas flow rate. Meanwhile, a vertical expansion should be due to a mass conservation, and the shape and overall upward movement of the bubble should be due to the buoyancy force acting on the bubble. Because of the upward movement of the bubble, the

plasma channel is exposed to a liquid surface at the bottom of the bubble. The water surface could easily absorb both the electrons from the plasma channel and the microwave power, resulting in the gradual quenching of the plasma.

In order to investigate physiochemical characteristics of the submerged MWPJ into water, we perform an optical emission spectroscopy. Light emission near the inlet of the MWPJ into the water container is collected using an optical fiber and analyzed using the spectrometer. Note that all the light emitted from the region inlet-water container is collected providing thus a time- and space-averaged measurements. The spectra presented in Fig. 5 are acquired by varying the μ WP, at a fixed Ar flow rate of 2 L/min and a fixed volume of water at 200 mL. The exposure time for each spectrum recorded is 1 ms, and 50 spectra are averaged for each tested μ WPs. As shown in Fig. 5, the OH (A–X) band and the Ar I lines are the most dominant emissions; H (α , β , and γ), O I, and NH (A–X) bands are also identified. Note that the NH emission, even with pure Ar, might be due to an impurity in the Ar or air dissolved into water. As μ WP increases, overall emission intensity also increases.

To estimate the rotational temperature of plasma particles (T_{rot}), we use the measured OH spectra by adopting the fitting method developed by Rodrigo et al. [29], and the results are shown in Fig. 6a, b. As a result, we find that the temperature increases from ~ 1300 to ~ 3200 K as the μ WP increases from 25 to 200 W (Fig. 6c). The reason that the rotational temperature is not proportional to the μ WPs is partly due to a higher heat loss for a condition with a higher temperature difference between the plasma channel and the surrounding media. It should be noted that the measured T_{rot} is in reasonable agreement with those values reported for microwave discharges at atmospheric pressure [30, 31].

Because the emission from OH radicals is dominant in the spectrum, we believe it is important to resolve its spatial origin and temporal dynamics. Using a narrow-band-pass optical filter centered at 309 nm (FWHM = 10 nm), we perform filtered imaging to spatially resolve the OH emission. Results presented in Fig. 7 are for various Ar flow rates, at μ WP = 200 W. The emission dynamics of OH, for an increasing Ar flow rate, are similar to those from the global emission previously discussed, showing distributed emission along

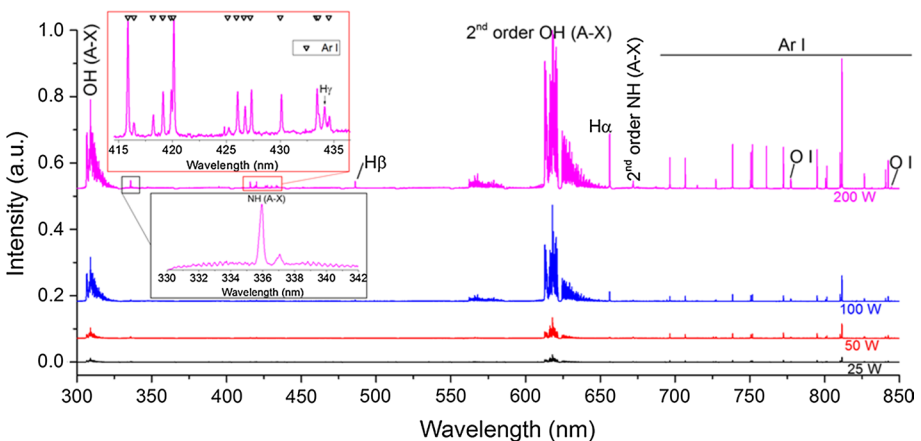


Fig. 5 Optical emission spectra acquired at the inlet of the MWPJ to the liquid cell for four μ WPs (25, 50, 100, and 200 W). Exposure time is 1 ms, each spectrum is averaged 50 measurements, Ar flow rate is 2 L/min, and the water volume is 200 mL

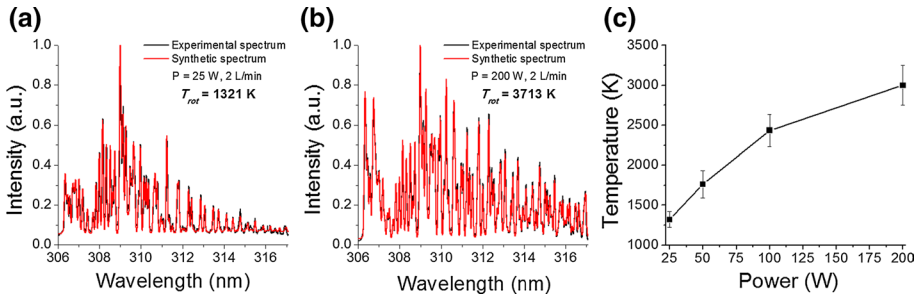


Fig. 6 Experimental and synthetic spectra of OH (A–X) at **a** 25 and **b** 200 W, respectively. **c** Rotational temperature variation as a function of μ WP; total Ar flow rate is 2 L/min and water volume is 200 mL

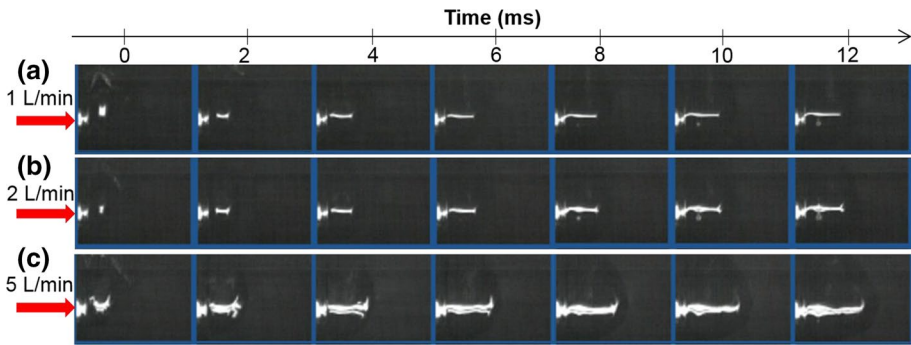


Fig. 7 Temporal dynamics of OH (309 ± 5 nm) emission for various Ar flow rates: **a** the argon flow rate of 1, **b** 2, and **c** 5 L/min. μ WP is 200 W and water volume is 200 mL. The red arrow indicates the plasma inlet and flow direction

the plasma channel. At 5 L/min, although the channel seems to be hollow, there is an actual filamentation, and the hollow structure is due to the inter-channels space.

Effects of Additive Nitrogen on the Submerged MWPJ

To further apply the submerged MWPJ for water treatment, we investigate the effects of gas additives to the Ar stream on the discharge dynamics. Here, we present the results obtained for N₂ only, omitting the results with oxygen and air because the bubble and plasma dynamics obtained for oxygen and air are found to be similar to those obtained with nitrogen. Figure 8 shows a selection of instantaneous images for two different N₂ percentages, 0.5 and 2%, respectively, for μ WP at 200 W, total gas flow rate of 2 L/min, and water volume of 200 mL. We find that the size of a bubble is not significantly affected by the percentage of N₂, since the size is mostly governed by the flow rate and thermodynamics. For 0.5% of N₂ (and for up to 1%), the change in the plasma length is insignificant compared to that observed for pure Ar. However, at 2% of N₂, the plasma length is significantly reduced, and with further addition of N₂ (e.g., at 5%), no plasma can be found in the bubble.

We analyze the lengths of the bubble and the discharge channel adopting the same method conducting in Fig. 3 to compare the plasma and bubble dynamics with the addition

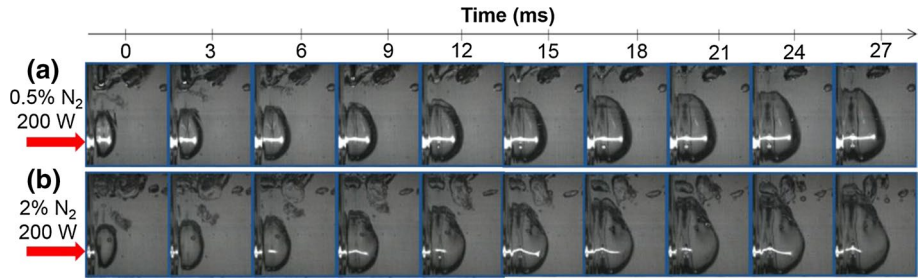


Fig. 8 Plasma–bubble dynamics for two N_2 percentages in Ar: **a** 0.5 and **b** 2%. μ WP is 200 W, total gas flow rate is 2 L/min, and water volume is 200 mL. The red arrow indicates the plasma inlet and flow direction

of N_2 . Results are presented in Fig. 9 for various percentages of N_2 in Ar flow comparing the corresponding pure Ar cases as a reference. As aforementioned, the change in the bubble length is negligible irrespective of N_2 portion. In terms of the plasma dynamics, we observe that, at 0.5% of N_2 , the increasing trend of the plasma length is similar to that of pure Ar, while it reaches its maximum length at ~ 50 ms, i.e., earlier than that with pure Ar (~ 65 ms). We also find that the duration of the plasma channel is similar to that obtained with pure Ar (Fig. 9a). At 1% of N_2 , the duration is also similar, but the retreating of the foremost discharge edge appears at ~ 45 ms (earlier than for 0.5% N_2), exhibiting a shorter maximum plasma length, ~ 6 mm, than that obtained with pure Ar, ~ 9 mm (Fig. 9b). For N_2 percentage higher than 1.5%, the typical monotonic increasing and decreasing behavior of the plasma length is not observed anymore. Particularly at 1.5% N_2 , it shows ‘hump and pit’ in its temporal trail demonstrating comparable maximum length of the plasma to that

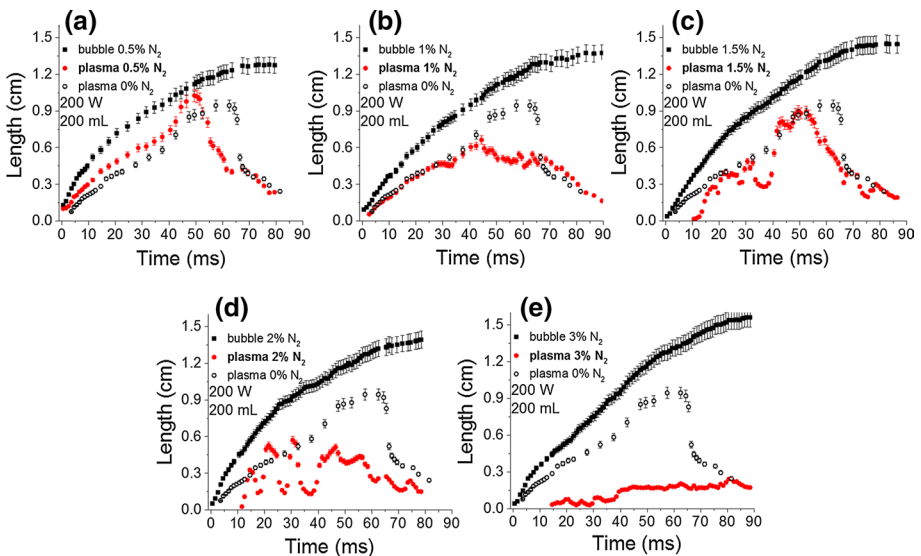


Fig. 9 Time evolution of the plasma and bubble lengths for various N_2 percentages in Ar flow: **a** 0.5, **b** 1, **c** 1.5, **d** 2, and **e** 3%. The plasma lengths at 0% N_2 (pure Ar) is superimposed each graph for comparison. Total gas flow rate is 2 L/min, μ WP is 200 W, and water volume is 200 mL

obtained with pure Ar (Fig. 9c). At 2% of N_2 , the oscillatory behavior of the plasma length is more pronounced showing multiple peaks in length (Fig. 9d). At 3% of N_2 , although some oscillations can be observed in the early stage, the oscillatory behavior seems to diminish after 40 ms accompanied by a significant reduction of the plasma channel in length. Finally, at 5% of N_2 , no discharge channel is observed in the bubble, but a tiny plasma close to surfatron can be observed.

The role of N_2 in plasma has been extensively studied for gas discharges at atmospheric pressure. It was reported, for example, that a significantly reduced plasma length was the result of the addition of N_2 . This could possibly be related to a high energy dissipation to the vibrational excitation of N_2 and/or a destruction of metastable Ar atoms by quenching reaction with N_2 and N_2^+ molecules [32]. It should be noted that no afterglow zone is observed in the submerged MWPI we investigated, although it is usually observed in discharges at atmospheric pressure once N_2 is added to Ar [30].

Figure 10 shows the variations of the optical emission spectra for a wavelength range of 300–400 nm, at various N_2 percentages. As a result of the addition of N_2 , we can identify emissions from NH, N_2 , and N_2^+ . Note that, once again, the NH emission for the case of pure Ar should be attributed to an impurity in the Ar or air dissolved into water. The emission intensity of NH (A–X) at 336 nm is drastically increased with the addition of N_2 showing comparable intensity to that of OH (A–X) at 309 nm. Higher intensities of both NH and OH emissions are obtained with smaller additions of N_2 , and increasing amount of N_2 leads to a degradation of the plasma generated radicals as shown in Fig. 9.

Undoubtedly, the source of OH radicals is water, and the formation of these radicals involves multiple pathways, which include an electron impact dissociation ($e + H_2O \rightarrow OH + H + e$), a dissociative electron attachment ($e + H_2O \rightarrow OH + H^-$), an electron–ion dissociative recombination ($e + H_2O^+ \rightarrow OH + H$ and $e + H_3O^+ \rightarrow OH + H_2$), a positive–negative ion recombination ($H^- + H_3O^+ \rightarrow OH + H_2 + H$), a dissociation with metastable atom ($Ar^* + H_2O \rightarrow OH + H + Ar$), and a charge exchange ($Ar^+ + H_2O \rightarrow OH + ArH^+$). Meanwhile, the NH emission can be magnified with the addition of N_2 . The effects of the additive N_2 on the Ar plasma kinetics in a gaseous system have been previously

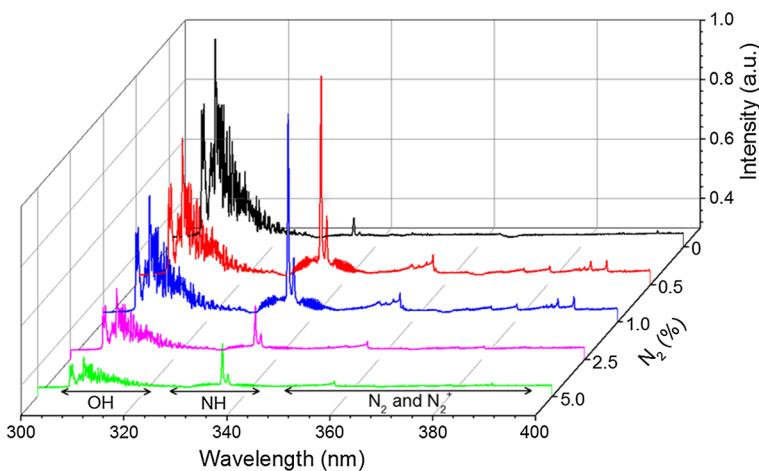


Fig. 10 Plasma optical emission spectra, in a range of 300–400 nm acquired at the inlet of the MWPI into the liquid container for various N_2 percentages. The integration time is 1 ms, and spectra are averaged over 50 measurements; μ WP is 200 W, total gas flow rate is 2 L/min, and water volume is 200 mL

investigated, both theoretically [33, 34] and experimentally [30]. In an Ar–N₂ gas mixture, a plasma generates nitrogen species, such as N, N₂^{*}, and N₂⁺, in various excited levels in addition to Ar^{*} and Ar⁺. Therefore, it is feasible that these chemically reactive species, together with electrons, effectively interact with the water vapor, which could then generate atomic and molecular species, such as H, O, and OH. The production of NH in N₂–H₂ has been investigated by Van Helden et al. [35], and they suggested the following formation mechanisms: N + H₂ → NH + H and/or N⁺ + H₂ → NH + H⁺. In fact, these reactions are proposed for N₂–H₂ plasma at conditions relatively far from those of our submerged MWPJ, where O and OH should be added to the proposed reactions. The formation of NH radicals in such conditions may indicate a complex chemistry in in-liquid plasma, but this needs to be further clarified by, for example, performing simulation studies.

Application to Methylene Blue Degradation

To assess a potential applicability of the submerged MWPJ to wastewater treatment, we select MB as a simulated organic contaminant. MB has been widely investigated in a water treatment field, which makes it suitable to draw valid comparisons. In the present study, we maintain a MB concentration at 50 mg/L. Figure 11 shows the normalized absorbance, which is obtained by the spectrophotometer, at 663 nm after 15 min of plasma processing for various gas mixtures (99% of Ar and 1% of O₂, air, or N₂, respectively) with a fixed μ WP = 200 W. Based on the relative absorbance values shown in the figure, we find that treatment performances (i.e., degree of decolorization) with Ar–N₂ and Ar–air mixtures are higher than those with other mixtures (Ar–O₂ and pure Ar). Since the decolorization with added oxygen is the least efficient, it can be concluded that nitrogen is a key factor in obtaining a greater performance with the Ar–air mixture. Thus, we further investigate the effect of the addition of N₂ on the decolorization process.

Figure 12 represents the variation of the absorbance at 663 nm (normalized to the case with pure Ar, i.e. 0% N₂) as a function of the percentage of N₂ in the gas mixture. In this figure, we clearly find that an optimum efficiency of the decolorization process is obtained for a nitrogen percentage of 2.5%. Based on the results obtained with emission intensities at various N₂ percentages in the pure water (Fig. 10), we postulate that an increase in NH radicals (for small additions of N₂) could play an important role in the decolorization process. In addition to the emitted energetic photons (wavelength 330–340 nm), NH radicals

Fig. 11 Normalized absorbance variation for MB in terms of gas mixture (99% of Ar and 1% of O₂, air, or N₂) after 15 min plasma processing; μ WP is 200 W, total gas flow rate is 2 L/min, and water volume is 200 mL. The absorbance is measured by the spectrophotometer

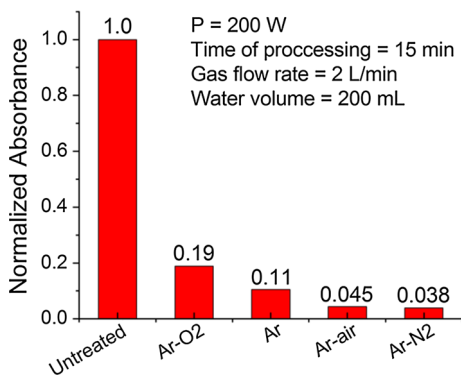
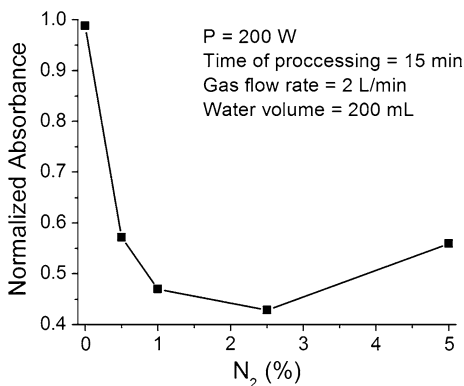


Fig. 12 Normalized absorbance for MB with respect to the pure Ar case (0% N₂) as a function of N₂ percentage in a Ar–N₂ gas mixture. The plasma processing time is 15 min, μ WP is 200 W, total gas flow rate is 2 L/min, and water volume is 200 mL. The absorbance is measured by the spectrophotometer



have a relatively high redox potential (~ 1 V) [36], therefore these may significantly contribute to the decomposition of MB.

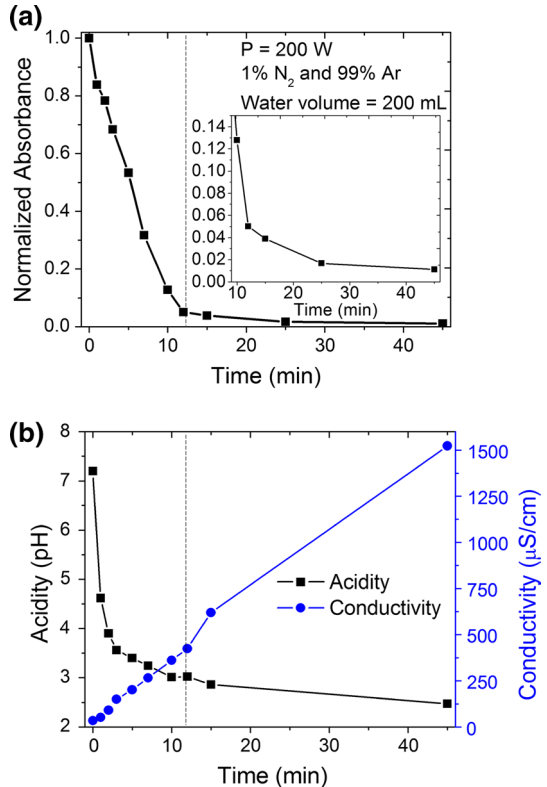
We should note that, with no addition of N₂, the OH radicals produced in the plasma are easily converted to H₂O₂ [1, 12], resulting in the deterioration of the oxidation potential of OH radicals. However, adding N₂ leads to the formation of NO and NO₂, which can significantly inhibit the consumption of OH radicals via the following backward reactions [12, 38]: H₂O₂ + NO \rightarrow HNO₂ + OH and H₂O₂ + NO₂ \rightarrow HNO₃ + OH. This secondary effect of N₂ addition may also create a favorable environment for the decomposition of MB. In fact, the induced chemistry in such a medium is very wide, and many other species that can contribute to MB degradation can be produced. For instance, water temperature increases significantly (to ~ 70 °C), and it has been observed, by Benetoli et al. [37], that dye decolorization increased with an increase in solution temperature. Also, other oxidizing species, such as peroxonitrous acid (ONOOH), can be produced in our conditions (e.g., H⁺ + NO₂⁻ + H₂O₂ \rightarrow ONOOH + H₂O) and can contribute to MB degradation [38].

We also investigate the normalized absorbance as a function of plasma processing time (Fig. 13a), at μ WP=200 W with 1% N₂. The trend of the change in the absorbance can be separated into two phases; the first phase, from 0 to 12 min, during which the absorbance exhibits a rapid drop resulting in a 95% reduction, and the second phase, from 12 to 45 min, during which the absorbance shows a slow decay. The time evolution of the absorbance is proportional to the concentration of MB in water. The evolution shows various slopes indicating therefore that there are different phases of the reaction that can be zero-, first-, and second-order.

We also study the time evolution of acidity and electrical conductivity of the plasma treated MB-contained water along the plasma processing time (Fig. 13b). During the first phase, from 0 to 12 min, we observe a fast decrease in the acidity, from ~ 7.2 to ~ 3 pH. During the second phase, from 12 to 45 min, the acidity slowly decreases from ~ 3 to ~ 2.5 pH. The time trend of the conductivity shows a linear increase from 10 to ~ 1500 μ S/cm. In fact, the acidity of the plasma treated MB-contained water is related to the concentration of H₃O⁺ in the solution, and the conductivity is related to the concentration of anions and cations in the solution. These ions can be created either by the by-products of the MB decomposition or by NO₂⁻ and NO₃⁻ produced in the plasma containing N₂.

We conduct additional experiments using pure distilled water (initial condition: conductivity=10 μ S/cm, acidity=7.2 pH) and compare the results of the acidity and the conductivity with those of MB-contained water (initial condition: conductivity=34 μ S/cm,

Fig. 13 Time evolution of **a** the absorption for MB and of **b** acidity and water conductivity; μ WP is 200 W, total gas flow rate is 2 L/min, and water volume is 200 mL



acidity = 7.2 pH). In this way, we are able to roughly distinguish the origins of ions dissolved in the water, which affect the decreased solution acidity and increased conductivity. Comparing the case A (pure distilled water) and the case C (distilled water treated by Ar plasma) in Fig. 14, the significant decrease in the acidity and increase in the conductivity can be attributed mainly to the production of H_3O^+ via the following reactions: $e + \text{H}_2\text{O} \rightarrow \text{H}_2\text{O}^+ + 2e$ then $\text{H}_2\text{O}^+ + \text{H}_2\text{O} \rightarrow \text{H}_3\text{O}^+ + \text{OH}$). For the case D (MB-contained water treated by Ar plasma) as compared to the case C, further increased conductivity and decreased acidity can be considered as a result of by-products from MB decomposition due to the plasma induced chemical reactions. To investigate the various reactions that can take place, a quantitative study should be conducted to identify and quantify the by-products in gas-phase as well as in liquid-phase. For the case E (distilled water treated by Ar-(1%)N₂ plasma), the increased conductivity and decreased acidity relative to the case C should be caused by ions originated by nitrogen, such as NO_2^- , NO_3^- , HNO_2 , and HNO_3 . Thus, the results with the case F (MB-contained water treated by Ar-(1%)N₂ plasma) should be attributed to the combined effects of H_3O^+ , NO_2^- , NO_3^- , and the by-product from MB decomposition.

Finally, we calculate the energy yield Y for MB decolorization using the following expression [28]:

$$Y \text{ (g/kWh)} = \frac{V(L)C_0(\text{g/L})\frac{C_0-C}{C_0}}{P(\text{kW}) \times t(\text{h})}$$

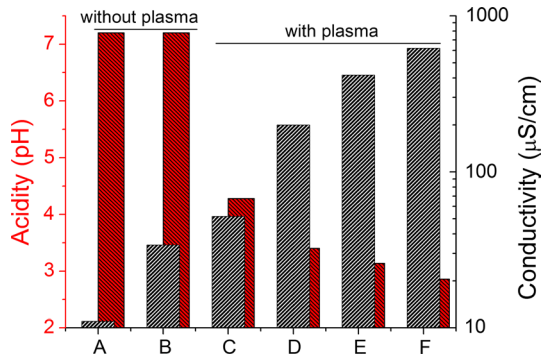


Fig. 14 Acidity and electrical conductivity of water before and after 15 min of plasma processing under various conditions of water and gas compositions; A (pure distilled water), B (MB contained distilled water), C (distilled water treated by Ar plasma), D (MB-contained distilled water treated by Ar plasma), E (distilled water treated by Ar-(1%)N₂ plasma), and F (MB contained distilled water treated by Ar-(1%)N₂ plasma). μ WP is 200 W, total gas flow rate is 2 L/min, and water volume is 200 mL

where V is the water volume, C_0 is the initial MB concentration, and C is the concentration of MB in the solution after treatment during a time t at power P . The yield to remove 50% of MB, $Y_{50\%}$, is thus estimated as 0.3 g/kWh. Table 1 provides a list of various plasma reactors used for MB removal as well as the $Y_{50\%}$. Compared to MWPJ in contact with water, the yield of the submerged one is 10 times higher (0.3 vs. 0.03). Pulsed corona discharges in-water with O₂ gas or in-contact with water with O₂ bubbles have the highest yield, i.e., 0.341 and 1.5, respectively.

Conclusion

We develop a submerged microwave plasma jet (MWPJ) system in water to enhance an applicability of plasmas in-liquid. It should have few advantages; (1) somewhat independent plasma generation of physical properties of liquid, (2) facilitated chemical process due to both electron- and thermally induced chemistry, (3) increased volume of plasma-liquid

Table 1 Energy yields to remove 50% of MB, $Y_{50\%}$, reported in various plasma reactors

MB concentration (mg/L)	Type of plasma reactor	$Y_{50\%}$ (g/kWh)	References
50	Submerged MWPJ	0.3	This work
50	MWPJ in contact with water	0.033	[28]
12	Diaphragm discharges	0.042	[39]
5	Radio-frequency discharges	0.037	[40]
10	Microwave discharges in water with air bubbling	0.155	[41]
13.25	Pulsed corona discharges in water with O ₂ bubbling	0.341	[42]
13	Pulsed corona discharges in water	0.064	[42]
15	O ₂ pulsed corona discharges in contact with water	1.5	[43]

interaction, and (4) turbulent mixing. Particularly, this proposed method has no influence of electrode erosion on treated liquids.

We investigate the physical characteristics of the submerged MWPJ in water. The plasma dynamics as well as the bubble dynamics are investigated using high-speed imaging, highlighting the effects of Ar flow rate and microwave power on them. We find that the plasma length increases with either increased gas flow rate or increased microwave power. Due to the anisotropic expansion of a gas bubble caused by horizontally injected MWPJ, a significant interaction between a plasma channel and the lower part of bubble-water interface can cause a retreating plasma channel resulting in its total extinction even before a bubble detachment from the inlet of MWPJ. We also show that the addition of N₂ to Ar highly affects the plasma dynamics exhibiting an extinction of plasma for the N₂ portion is higher than 5% while, at the percentage < 5%, an oscillatory behavior of the discharge channel is found. A characterization by an optical emission spectroscopy shows that, in the case of Ar plasma, the spectrum is dominated by OH (A–X) band and by Ar I lines, including discernable H (α , β , and γ), O I, and the NH (A–X) band, indicating effective dissociation of water via plasma chemistry. As a result of N₂ addition, an intense emission of NH is observed with additional excited N₂ and N₂⁺ emissions.

In order to assess the feasibility of the submerged MWPJ in liquid chemical processes, we perform a wastewater treatment experiment by selecting methylene blue as a model organic contaminant. We compare the decolorization performance by changing additive gas (N₂, O₂, and air) to Ar. As a result, we find that N₂ is the most effective additive among tested, due to the backward reactions of H₂O₂ to produce OH radicals caused by NO and NO₂ as well as a potential redox capability of NH radicals. Particularly, we show that the addition of 1–3% of N₂ increases the decolorization efficiency exhibiting more than 90% of MB is decomposed during the first 10 min of processing for the initial MB concentration of 50 mg/L. This result shows that the submerged MWPJ can be used for efficient in-liquid chemical processes, avoiding an issue with electrode erosion encountered in other plasma devices.

Acknowledgements The research reported in this publication was supported by funding from King Abdulah University of Science and Technology (KAUST), under Award Number BAS/1/1384-01-01.

References

1. Locke BR, Shih KY (2011) Review of the methods to form hydrogen peroxide in electrical discharge plasma with liquid water. *Plasma Sources Sci Technol* 20(3):034006
2. Lebedev YA (2017) Microwave discharges in liquid dielectrics. *Plasma Phys Rep* 43(6):685
3. Foster JE (2017) Plasma-based water purification: challenges and prospects for the future. *Phys Plasmas* 24(5):055501
4. Ceccato PH, Guaitella O, Le Gloahec MR, Rousseau A (2010) Time-resolved nanosecond imaging of the propagation of a corona-like plasma discharge in water at positive applied voltage polarity. *J Phys D Appl Phys* 43(17):175202
5. Hamdan A, Cha MS (2016) Low-dielectric layer increases nanosecond electric discharges in distilled water. *AIP Adv* 6(10):105112
6. Marinov I, Starikovskaia S, Rousseau A (2014) Dynamics of plasma evolution in a nanosecond underwater discharge. *J Phys D Appl Phys* 47(22):224017
7. Laurita R, Barbieri D, Gherardi M, Colombo V, Lukes P (2015) Chemical analysis of reactive species and antimicrobial activity of water treated by nanosecond pulsed DBD air plasma. *Clin Plasma Med* 3(2):53–61
8. Tian W, Kushner MJ (2014) Atmospheric pressure dielectric barrier discharges interacting with liquid covered tissue. *J Phys D Appl Phys* 47(16):165201

9. Robert E, Darny T, Dozias S, Iseni S, Pouvesle JM (2015) New insights on the propagation of pulsed atmospheric plasma streams: from single jet to multi jet arrays. *Phys Plasmas* 22(12):122007
10. Surov AV, Popov SD, Popov VE, Subbotin DI, Serba EO, Spodobin VA, Nakonechny GV, Pavlov AV (2017) Multi-gas AC plasma torches for gasification of organic substances. *Fuel* 203:1007–1014
11. Chang JS (2001) Recent development of plasma pollution control technology: a critical review. *Sci Technol Adv Mater* 2(3–4):571–576
12. Liu JL, Park HW, Hamdan A, Cha MS (2018) In-liquid arc plasma jet and its application to phenol degradation. *J Phys D Appl Phys* 51:114005
13. Liedtke KR, Bekeschus S, Kaeding A, Hackbarth C, Kuehn JP, Heidecke CD, Bernstorff W, Woedtke T, Partecke LI (2017) Non-thermal plasma-treated solution demonstrates antitumor activity against pancreatic cancer cells in vitro and in vivo. *Sci Rep* 7(1):8319
14. Tanaka H, Ishikawa K, Mizuno M, Toyokuni S, Kajiyama H, Kikkawa F, Metelmann HR, Hori M (2017) State of the art in medical applications using non-thermal atmospheric pressure plasma. *Rev Mod Plasma Phys* 1(1):3
15. Magureanu M, Mandache NB, Parvulescu VI (2015) Degradation of pharmaceutical compounds in water by non-thermal plasma treatment. *Water Res* 81:124–136
16. Hamdan A, Marinov I, Rousseau A, Belmonte T (2013) Time-resolved imaging of nanosecond-pulsed micro-discharges in heptane. *J Phys D Appl Phys* 47(5):055203
17. Hamdan A, Cha MS (2015) Ignition modes of nanosecond discharge with bubbles in distilled water. *J Phys D Appl Phys* 48(40):405206
18. Hamdan A, Cha MS (2016) The effects of gaseous bubble composition and gap distance on the characteristics of nanosecond discharges in distilled water. *J Phys D Appl Phys* 49(24):245203
19. Hamdan A, Noel C, Kosior F, Henrion G, Belmonte T (2013) Impacts created on various materials by micro-discharges in heptane: influence of the dissipated charge. *J Appl Phys* 113(4):043301
20. Hamdan A, Kabbara H, Noël C, Ghanbaja J, Redjaimia A, Belmonte T (2018) Synthesis of two-dimensional lead sheets by spark discharge in liquid nitrogen. *Particuology*. <https://doi.org/10.1016/j.partic.2017.10.012>
21. Belmonte T, Hamdan A, Kosior F, Noël C, Henrion G (2014) Interaction of discharges with electrode surfaces in dielectric liquids: application to nanoparticle synthesis. *J Phys D Appl Phys* 47(22):224016
22. Tu Y, Xian Y, Yang Y, Lu X, Pan Y (2017) Time-resolved imaging of electrical discharge development in multiple bubbles immersed in water. *Plasma Process Polym* 14(10):1600242
23. Hamdan A, Cha MS (2016) Nanosecond discharge in bubbled liquid *n*-heptane: effects of gas composition and water addition. *IEEE Trans Plasma Sci* 44(12):2988–2994
24. Zhang X, Cha MS (2015) The reformation of liquid hydrocarbons in an aqueous discharge reactor. *J Phys D Appl Phys* 48(21):215201
25. Dai XJ, Corr CS, Ponraj SB, Maniruzzaman M, Ambujakshan AT, Chen Z, Kviz L, Lovett R, Rajmohan GD, de Celis DR, Wright ML (2016) Efficient and selectable production of reactive species using a nanosecond pulsed discharge in gas bubbles in liquid. *Plasma Process Polym* 13(3):306–310
26. Tian W, Tachibana K, Kushner MJ (2013) Plasmas sustained in bubbles in water: optical emission and excitation mechanisms. *J Phys D Appl Phys* 47(5):055202
27. Barkhudarov EM, Kossyi IA, Misakyan MA, Taktakishvili IM (2012) New microwave plasma source in water. In: Lebedev YA (ed) *Microwave discharges: fundamentals and applications*. Yanus-K, Moscow, p 43
28. García MC, Mora M, Esquivel D, Foster JE, Rodero A, Jiménez-Sanchidrián C, Romero-Salguero FJ (2017) Microwave atmospheric pressure plasma jets for wastewater treatment: degradation of methylene blue as a model dye. *Chemosphere* 180:239–246
29. Cardoso RP, Belmonte T, Keravec P, Kosior F, Henrion G (2007) Influence of impurities on the temperature of an atmospheric helium plasma in microwave resonant cavity. *J Phys D Appl Phys* 40(5):1394
30. Bravo JA, Rincón R, Muñoz J, Sánchez A, Calzada MD (2015) Spectroscopic characterization of argon–nitrogen surface-wave discharges in dielectric tubes at atmospheric pressure. *Plasma Chem Plasma Process* 35(6):993–1014
31. Chen CJ, Li SZ, Zhang J, Liu D (2017) Temporally resolved diagnosis of an atmospheric-pressure pulse-modulated argon surface wave plasma by optical emission spectroscopy. *J Phys D Appl Phys* 51(2):025201
32. Itikawa Y (2006) Cross sections for electron collisions with nitrogen molecules. *J Phys Chem Ref Data* 35(1):31–53
33. Bogaerts A (2009) Hybrid Monte Carlo—fluid model for studying the effects of nitrogen addition to argon glow discharges. *Spectrochim Acta Part B* 64(2):126–140

34. Henriques J, Tatarova E, Guerra V, Ferreira CM (2002) Wave driven N_2 -Ar discharge. I. Self-consistent theoretical model. *J Appl Phys* 91(9):5622–5631
35. Van Helden JH, Van den Oever PJ, Kessels WMM, Van de Sanden MCM, Schram DC, Engeln R (2007) Production mechanisms of NH and NH_2 radicals in N_2 - H_2 plasmas. *J Phys Chem A* 111(45):11460–11472
36. Jonsson M, Lind J, Merényi G, Eriksen TE (1995) N–H bond dissociation energies, reduction potentials and pK_as of multisubstituted anilines and aniline radical cations. *J Chem Soc Perkin Trans 2*(1):61–65
37. Benetoli LODB, Cadorin BM, Postiglione CDS, Souza IGD, Debacher NA (2011) Effect of temperature on methylene blue decolorization in aqueous medium in electrical discharge plasma reactor. *J Braz Chem Soc* 22(9):1669–1678
38. Moussa D, Doubla A, Kamgang-Youbi G, Brisset JL (2007) Postdischarge long life reactive intermediates involved in the plasma chemical degradation of an azoic dye. *IEEE Trans Plasma Sci* 35(2):444–453
39. Stará Z, Krčma F, Nejezchleb M, Skalný JD (2009) Organic dye decomposition by DC diaphragm discharge in water: effect of solution properties on dye removal. *Desalination* 239(1–3):283–294
40. Maehara T, Miyamoto I, Kurokawa K, Hashimoto Y, Iwamae A, Kuramoto M, Yamashita H, Mukasa S, Toyota H, Nomura S, Kawashima A (2008) Degradation of methylene blue by RF plasma in water. *Plasma Chem Plasma Process* 28(4):467–482
41. Ishijima T, Hotta H, Sugai H, Sato M (2007) Multibubble plasma production and solvent decomposition in water by slot-excited microwave discharge. *Appl Phys Lett* 91(12):121501
42. Malik MA, Ghaffar A, Ahmed K (2002) Synergistic effect of pulsed corona discharges and ozonation on decolorization of methylene blue in water. *Plasma Sources Sci Technol* 11(3):236
43. Ikoma S, Satoh K, Itoh H (2009) Decomposition of methylene blue in an aqueous solution using a pulsed-discharge plasma at atmospheric pressure. *IEEJ Trans Fundam Mater* 129:237–244